Coded Aperture Raman Spectroscopy for Quantitative Measurements of Ethanol in a Tissue Phantom

S. T. McCAIN, M. E. GEHM, Y. WANG, N. P. PITSIANIS, and D. J. BRADY*

Department of Electrical and Computer Engineering and the Fitzpatrick Institute for Photonics, Duke University, Durham, North Carolina 27708

Coded aperture spectroscopy allows for sources of large étendue to be efficiently coupled into dispersive spectrometers by replacing the traditional input slit with a patterned mask. We describe a coded aperture spectrometer optimized for Raman spectroscopy of diffuse sources, (e.g., tissue). We provide design details of the Raman system, along with quantitative estimation results for ethanol at non-toxic levels in a lipid tissue phantom. With 60 mW of excitation power at 808 nm, leave-one-out and blind cross-validation of partial least squares (PLS) regression models achieve $r^2 > 0.98$. Leave-one-out cross-validation demonstrates prediction errors of <15% at the common legal limit for intoxication (17.4 mmol/L = 0.08% by vol) and the best blind cross-validation achieves <12% error at this concentration.

Index Headings: **Raman spectroscopy; Multiplexing; Chemometrics.**

INTRODUCTION

Raman spectroscopy is a powerful diagnostic tool as result of its high specificity and potential for *in vivo* measurement.[1] At the same time, its very weak cross-section and incoherent scattering properties make the Raman signal challenging to detect. With the advent of high-performance charge-coupled device (CCD) detectors, near-infrared (NIR) diode lasers, and high-throughput spectrographs, systems have been demonstrated that detect various biological analytes at physiological levels in aqueous humor, urine, and filtered blood serum.[2–4] In highly-scattering media like blood and tissue, Raman-based diagnostics are more challenging, but *in vivo* applications are becoming more realizable with recent progress in instrumentation and data analysis.[5–7] The difficulty in working with highly scattering samples arises from the fact that the source has a larger étendue than can be measured by traditional spectrometers.

We have designed and constructed a coded-aperture Raman spectrometer that uses multimodal multiplex spectroscopy (MMS) to achieve a larger étendue than comparable slit-based systems. Such aperture coding has been explored previously under the terms "multi-channel spectroscopy"[8] and "Hadamard transform spectroscopy" (HTS).[9]

Initially, HTS systems were designed to use multiplexing to overcome the noisy characteristics of single-channel detectors for imaging and spectroscopy.[8,10–13] Modifying a dispersive spectrometer by placing a patterned mask in the input aperture and at the detector allowed for both the multiplex and throughput advantage.[9] By scanning the mask at the detector, one-dimensional (1D) spectra could be obtained, or scanning both masks allowed for a two-dimensional (2D) data set with one spatial and one spectral dimension.

With the advent of multi-channel detectors, high-throughput multiplexed imaging spectrometers were developed with the use of liquid crystal spatial light modulators[14,15] and micro-electromechanical systems (MEMS) arrays.[16] In both systems, a three-dimensional data set (two spatial and one spectral) was formed by processing multiple images, each taken with a different spatial multiplexing code.

When a source is diffuse, however, spatial multiplexing can allow for the static measurement of the spectrum with limited spatial information. Such an approach was shown to be effective at obtaining a spectrum of a diffuse source by replacing the slit of a spectrometer with a multiple-slit mask and then performing a 1D deconvolution of the detector data.[17] This approach suffers, however, from not being as well conditioned computationally as the multiple measurement methods.

In our described (MMS) design, the slit in the input aperture of a dispersive spectrograph is replaced by a 2D pattern of openings based on the Hadamard matrices. The input aperture is divided into many vertical sub-apertures, which are open and closed in various combinations on each column of the mask. By assuming uniformity of the source along the columns of the mask, all the measurements can be made in parallel on a 2D detector array and a single-shot reconstruction is possible. For the diffuse sources encountered in highly scattering media such as tissue, this assumption is valid.

The reconstructed data forms a 2D data set (one spatial and one spectral), with the spatial dimension corresponding to the portion of the source incident on each column of the aperture mask. The spectral estimates for each column can then be further shifted and summed in order to provide an average spectrum of the 2D source, allowing for a signal-to-noise ratio (SNR) gain of $\sqrt{N/2}$, where N is the order of the Hadamard matrix used. This gain arises solely due to the increased throughput, and we have experimentally verified this in a previous paper.[18] A further multiplex advantage can also be realized in the presence of detector noise due to the increased signal on the detector elements.

While the previous discussion applies generally to MMS systems, this manuscript will focus on the specific implementation of a Raman MMS system designed to measure ethanol concentrations in a tissue phantom. The described system is able to measure the average spectrum of an extended source statically with a large input aperture (40% of the 7.47 mm^2 input aperture), while not sacrificing resolution (full-width at half-maximum (FWHM) $\sim$ 0.58 nm). The étendue of the system is approximately 12 times that of a slit-based system with an equivalent resolution and input aperture height. The input aperture codes allow for a rapid (<1 s), well-conditioned deconvolution of the detector data.

We have demonstrated the detection of ethanol in solutions of a highly scattering tissue phantom at non-toxic concentrations. Through partial least squares (PLS) regression, concentration estimation of alcohol is shown to achieve r^2 values of >0.98

Received 22 November 2005; accepted 22 March 2006.

* Author to whom correspondence should be sent. E-mail: dbrady@duke.edu.

0003-7028/06/6006-0663$2.00/0

and prediction errors of <15% at a common legal limit of alcohol concentration (17.4 mmol/L = 0.08% by vol).

MULTIMODAL MULTIPLEX SPECTROSCOPY OF DIFFUSE SOURCES

As mentioned above, spectroscopic sources of large angular and spatial extent are difficult to couple efficiently into dispersive spectrometers, since the étendue of the source is larger than that of the spectrometer. In this section, we will describe how the physics of photon scattering naturally leads to sources of large étendue in biological systems. We then summarize the theory of MMS spectroscopy and show how it can be used to measure such diffuse sources. We have previously published a more detailed version of this theory.[18]

Light Scattering by Tissue. In optical tissue diagnostics, the NIR regime is typically chosen due to the low absorption by tissue components. In Raman spectroscopy, it is also advantageous as a result of the reduced intensity of the background fluorescence. In this wavelength region in tissue such as skin, scattering rather than absorption dominates photon transport and thus the diffusion approximation can be made. The time-independent diffusion can be expressed as[19]

$$\nabla^2\Phi_d(r) - \kappa_d^2\Phi_d(r) = 0 \tag{1}$$

where Φ_d is the photon fluence, r is the radial distance from the source, and $1/\kappa_d$ is the diffusion length. The diffusion length can be expressed as

$$\frac{1}{\kappa_d} = \left\{\frac{1}{3\mu_a[\mu_a + \mu_s(1-g)]}\right\}^{1/2} \tag{2}$$

The scattering and absorption constants, μ_s and μ_a, respectively, as well as g, the anisotropic scattering parameter, are readily available for various biological components.[19] In order to roughly estimate the photon distribution in tissue, the solution for a point source is used:

$$\frac{\Phi_d(r)}{h\nu c_m} = \frac{N\kappa_d^2}{4\pi}\frac{\exp(-\kappa_d r)}{r} \tag{3}$$

Here N is the number of injected photons and c_m is the phase velocity in the medium. This equation is explicitly integrated to determine the approximate photon distribution of light as a function of the material parameters. The solution can be expressed as

$$N(r) = N_{tot}[1 - (1 + \kappa_d r)\exp(-\kappa_d r)] \tag{4}$$

To accurately calculate the distribution of the Raman photons requires a simulation that includes the Raman cross-sections of tissue components and the boundary conditions of the medium. However, to a good approximation, the Raman photon density is proportional to the excitation photon density. In place of a simulation, an experiment was performed using a Ti:Sapphire laser and a photodiode array to measure the remitted photon distribution of a human forearm. A calibrated linear array of CCD detectors pushed up against the skin was used to measure the remitted light of the laser at 840 nm. The percentage of the total remitted light distribution is shown, along with calculated photon distributions in Fig. 1. Clearly, for skin, there is an excellent agreement between the model and experiment.

From the model, we find that in blood the photons stay relatively localized, with 90% of the photons staying within 1 millimeter of the excitation source. However in tissue the spot size of the radiation vastly increases: only 25% of the photons are distributed within 1 millimeter of the source.

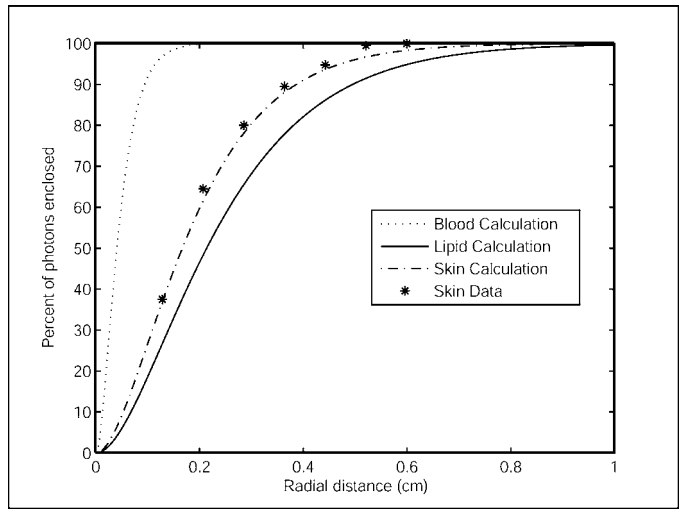

FIG. 1. The percentage of enclosed photons as a function of radial distance from a point source is shown for the scattering-dominant limit in a uniform medium. The tissue phantom has $\mu_a = 0.23\ cm^{-1}$, $\mu_s = 217.5\ cm^{-1}$, and $g = 0.589$.[26] The blood model has $\mu_a = 12.5\ cm^{-1}$, $\mu_s = 22.2\ cm^{-1}$, and $g = 0.99$.[28] The skin model has $\mu_a = 0.63\ cm^{-1}$, $\mu_s = 265\ cm^{-1}$, and $g = 0.8$.[19]

Theory of Multimodal Multiplex Spectroscopy. Dispersive spectroscopy of diffuse sources is challenging because of their incoherent nature. This means radiation from the source can not be focused or have its local brightness increased.[20] Thus, to achieve a given spectral resolution, the experimenter is faced with three possibilities:

(1) Allow the input slit of the spectrometer to act as a spatial filter and thus reject the majority of the available photons.
(2) Use a structured fiber bundle or other non-imaging technique to remap the diffuse source into a slit shape.
(3) Remove the slit entirely and deconvolve the spectra using a known instrument response function.
(4) Design a coded aperture spectrometer with an input aperture matched to the size of the source.

For weak, diffuse sources, such as those common in biological systems, the first option will result in a photon starved measurement and extremely poor SNR. In the second option, to avoid rejecting photons, the resulting slit must have the same area as the original source. In order to completely couple large sources, this can result in slit lengths that are unreasonable. Further, the method introduces fiber coupling and transmission losses. However, despite these problems, it is a straightforward approach that is favored by many leading research groups.[5,21,22]

Another option is to remove the slit entirely and then digitally post-process the 2D detector data in order to remove the blurring due to the wide input aperture. This approach has been shown to be only moderately effective for either spectrally sparse or spatially uniform sources, since artifacts are present due to the ill-conditioned nature of the problem.[23]

We choose the last option, and have designed a multimodal multiplex spectrometer that is capable of simultaneous high-resolution and high-throughput measurements of sources of large étendue. *Multimodal* indicates that the system accepts

a large number of spatial and angular modes, while *multiplex* indicates that signals are combined on the detector plane, thereby increasing the average flux and providing an SNR gain in the presence of detector noise.

A schematic of an MMS system is shown in Fig. 2. Internal optical elements form an image of the input aperture at wavelength-dependent locations on the detector plane. The detected intensity pattern is the convolution of the spectrum of the source with the input aperture.

Mathematically, we can write the intensity at the detector plane as

$$I(x', y') = \iiint \delta\{x - [x' + \alpha(\lambda - \lambda_c)]\} \times \delta(y - y')T(x, y)S(x, y; \lambda)\mathrm{d}x\,\mathrm{d}y\,\mathrm{d}\lambda \quad (5)$$

Here, $\delta\{x - [x' + \alpha(\lambda - \lambda_c)]\}$ is the propagation kernel for a dispersive grating spectrometer of unity magnification with linear dispersion α in the x-direction, and a center wavelength of λ_c for an aperture at $x = 0$ for all y. $T(x, y)$ is the transmission function of the input aperture and $S(x, y; \lambda)$ is the spectral density of the source at the aperture plane. For a source that is uniform in x and y, this reduces to

$$I(x', y') = \int T(x, y')S\left(\lambda = \frac{x - x'}{\alpha}\right)\mathrm{d}x \quad (6)$$

where $S(\lambda)$ is now the spatially uniform spectrum. Note that this equation is the previously mentioned convolution of the spectrum with the input aperture. This convolution is ambiguous with respect to the light's entrance position and wavelength. The goal of spectroscopy is to break this ambiguity.

In a traditional slit based system, the aperture function $T(x, y)$ is approximated as $T(x, y) \approx \delta(x)$, which breaks the ambiguity and leads to an isomorphic relationship between output position and wavelength. However, for extended sources, this results in a large reduction in throughput, as mentioned previously. In contrast, an MMS system uses an extended aperture pattern that has been designed such that the ambiguity can be broken with digital post-processing of the detector data. A $T(x, y)$ is chosen such that there exists an analysis function $\hat{T}(x, y)$ where

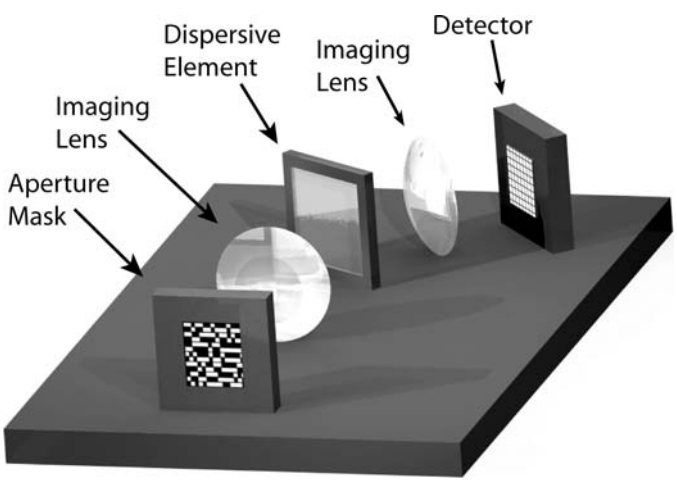

FIG. 2. Optical layout of the coded aperture MMS. The conventional slit of a dispersive spectrometer is replaced with a coded aperture to allow for high throughput without a reduction of resolution. The detector data is digitally post-processed into an average spectrum of the source.

$$\int T(x, y)\hat{T}(x', y)\mathrm{d}y \approx \delta(x - x') \quad (7)$$

A more thorough discussion of MMS theory, as well as a derivation of a number of aperture code patterns, can be found in our earlier paper.[18]

Heuristically, the coding procedure can be thought of as dividing the columns of the input aperture into many "virtual slits". These slits are then coded orthogonally using the columns of a Hadamard matrix. During post-processing, each column of the detector data is then inverted using the same Hadamard matrix in order to reconstruct the individual spectra resulting from each slit.

This heuristic model leads to two important realizations about the system. First, the source needs to be uniform along each column since the data is inverted in a column-wise fashion. Along the row-wise dimension, the system performs as a 1D spectral imager. For this investigation, only the average spectrum is desired, and thus the spectra from the sub-apertures are averaged. This property could be exploited, however, to perform depth selectivity similar to previous work on spatially offset Raman spectroscopy.[7] Since ethanol diffuses readily throughout tissue,[24] however, its depth dependence is assumed to be negligible.

The second realization from the virtual slit view involves the spectral range of the instrument. While the spectral range spanned in the reconstruction will be the spectral channels observed by both the slits on the edges of the aperture mask, only the region of the spectra that is measured by all the slits will have the $N/2$ throughput advantage. The spectral channels at the edges will have a fewer number of estimates the further they are from the edges defined by the union of all the estimates.

System Design and Performance. In this section we describe an MMS Raman system for chemometrics of tissue. While this system was primarily composed of research grade components in order to fully explore the detection limit of weak analytes in tissue, MMS systems have been demonstrated in our laboratory using inexpensive webcams, reflective gratings, mask orders between 12 and 48, and broad spectral ranges.

For the described system, excitation at 808 nm provides low background autofluorescence and puts the chemical fingerprint region of Raman features (500-2000 cm^{-1}) at $\simeq$840–960 nm, within the high quantum efficiency range of our CCD. The illumination portion delivers light to the sample cuvettes and relays the Raman scattered light to the spectrometer. The spectrometer portion consists of an aperture mask with a spectrograph and a cooled CCD.

Optical Design. The optical layout of the system is shown in Fig. 3. The excitation source is a butterfly packaged, fiber-coupled, single longitudinal- and transverse-mode semiconductor diode laser (QPhotonics QFLD-808-100S) operating at 808 nm with 60 mW incident on the sample. The butterfly package is current- and temperature-regulated, but there is no external stabilization of the laser wavelength, resulting in a linewidth of $\approx$0.3 nm.

The output of the laser is collimated with a short focal length plastic lens and passes through a thin-film bandpass filter (Omega Optical custom: transmits 800–810 nm otherwise optical density of 5) to reject out-of-band spontaneous emission. The relay section of the system provides two functions: delivering the excitation laser light to the sample, and relaying the scattered light from the sample to the aperture

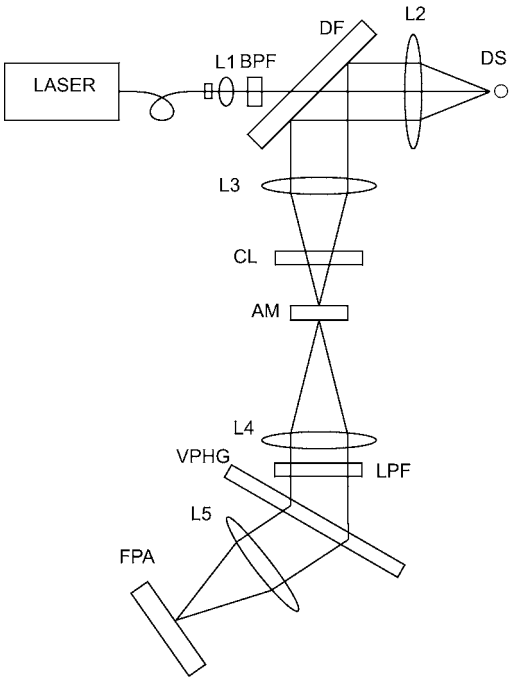

FIG. 3. The schematic of the Raman MMS system. The excitation laser light passes through the band-pass filter (BPF), is then collimated by a lens (L1), transmitted through the dichroic filter (DF), and then focused on to the sample by a lens (L2). The diffuse source (DS) is then imaged onto the aperture mask (AM) by two lenses (L2, L3) and the reflection by the dichroic filter (DF). The cylindrical lens (CL) Fourier transforms the source vertically to achieve uniform illumination across the mask columns. The aperture mask then serves as the input to the spectrograph, consisting of two lenses (L4, L5), which image the aperture mask onto the focal plane array (FPA) after passing through a long-pass filter (LPF) to reduce the Rayleigh scattered excitation light and the volume phase holographic grating (VPH) to disperse the source along the rows of the focal plane array.

mask. The excitation light passes through a rectangular dichroic filter (Omega Optical custom: transmits 800–810 nm, reflects 850–950 nm in a 45° geometry), and is focused onto the sample by an *f*/1 lens to a spot of ≈200 μm. The scattered light from the source is collimated by the same *f*/1 lens, reflected off the dichroic filter and imaged onto the aperture mask by an *f*/2 lens. The lenses provide a 52° collection full-angle at the sample, and then magnify the source 2× onto the mask. This matches the angular extent of the source to the spectrograph (*f*/2). A 100 mm focal length cylindrical lens is placed between the final relay lens and the aperture mask in order to Fourier transform the field in the *y*-direction to improve spatial uniformity. Since the aperture code assumes uniform spectra along the columns, a much better reconstruction fidelity is seen with such an anamorphic setup for weakly scattering samples. For highly scattering samples there is a negligible effect on the fidelity.

The patterned mask, described later, then forms the input aperture of a home-built axial transmissive Raman spectrograph with a center wavelength of 900 nm. The design goal of the spectrograph was to have high throughput, moderate spectral resolution, and sufficient image quality to easily resolve the mask features. A transmissive volume phase holographic grating (Wasatch Photonics) with 1000 line pairs per millimeter provides the dispersion. Combining the grating with two *f*/1.4 lenses (Pentax B7514C) and the 54 μm minimum mask feature size, results in an overall *f*/2.1 system with ≃0.6 nm over the 4.30 mm × 1.73 mm input aperture. The spectral range of interest, 850–950 nm, under-fills the detector plane in the dispersion direction in order that every spectral estimate is fully sampled by the detector plane.

A long-pass filter (Omega Optical), 850–1000 nm pass-band with optical density of 6 at the laser wavelength, provides rejection of the Rayleigh scattered laser light. The focal plane detector is a deep-depletion back-illuminated CCD array (Andor Technologies DU440-BR-DD), with a 2048 × 512 array of 13.5 μm square pixels. The high-resolution CCD allows for higher-order masks to be used in the system. The camera is operated at −60 °C to decrease the high dark current that is common with deep depletion CCDs. No water cooling or liquid nitrogen is required to keep the CCD stabilized at this temperature. The dark current at this temperature is ≈ $1e^-$/pix/s; however, the signal counts per pixel from sample autofluorescence are at least two orders of magnitude higher.

Aperture Coding. For this instrument we used the row-doubled Hadamard codes described in our previous work.[18] The aperture mask is lithographically patterned chrome on quartz (Applied Image Group), allowing for >90% transmission and a blocking optical density of ≈ 4. An $N = 32$ row-doubled Hadamard code with 54 μm square features allows for a system resolution of ≃0.6 nm. A scale replica of the code is shown in Fig. 4. The rows and columns of the row-doubled Hadamard code are randomly permuted to reduce spurious correlations observed in earlier experiments. There is a 4:1 ratio between the mask feature size and the CCD pixel size. This avoids the need for sub-pixel positioning accuracy of the mask. Completely opaque rows of 1 CCD pixel height are placed between each row in the code. These *dead rows* reduce cross-talk between adjacent codes of the mask, resulting from the point spread function (PSF) of the optical system. The height of the mask is thus $(2N \times 4 + 2N - 1) \times 13.5\ \mu\text{m} = 4.30$ mm. The width of the mask is simply $N \times 4 \times 13.5\ \mu\text{m} = 1.73$ mm. Since the row-doubled Hadamard codes average half open, and the dead rows reduce the average vertical throughput by 20%, the total open area is 2.98 mm^2. To achieve a similar collection area in a slit-based spectrometer that uses a fiber to remap the source would require a slit height of 55 mm, if the resolution of the two systems were equal. Clearly this is significantly larger than typical detector arrays, and as such,

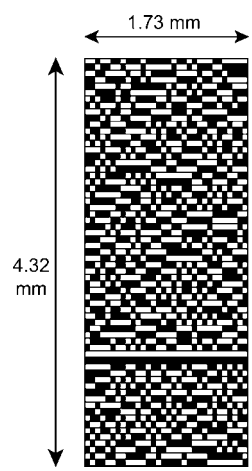

FIG. 4. Row-doubled, shuffled, $N = 32$ Hadamard mask, with 54 μm square features.

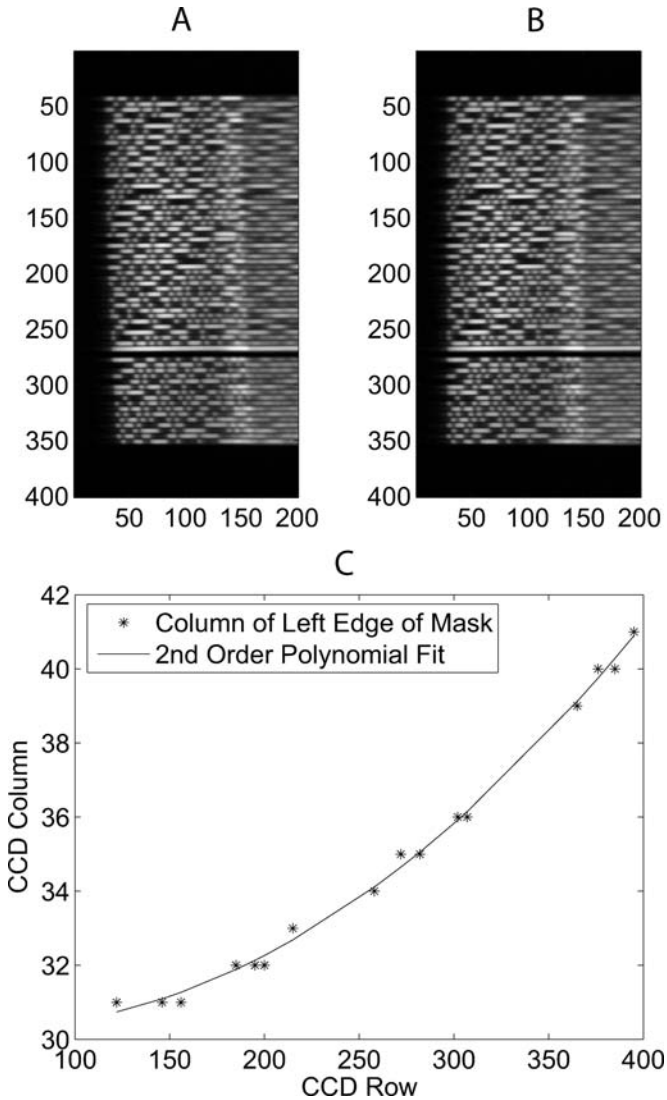

FIG. 5. (**A**) Raw data from the CCD that exhibits smile distortion. (**B**) Shifted data after curvature correction. (**C**) Polynomial least squares fit of image curvature used to determine the amount of shift needed for each row.

only a coded-aperture system could achieve a collection area of this size.

Spectral Estimation/System Calibration and Performance. The two-dimensional CCD intensity data from the CCD is digitally post-processed to recover a one-dimensional average spectrum of the source. In order to be able to calibrate various parameters of the reconstruction, a cuvette of pure cyclohexane is analyzed. The Raman features of cyclohexane are very narrow, which allows for high fidelity reconstruction parameters. This calibration data is then saved and used for reconstructions of unknown sources.

A portion of the CCD intensity image is shown in Fig. 5A. The *smile distortion*[25] of the CCD image in the x-direction is apparent, and must be corrected in order to preserve the registration of the mask rows. The left edge of the mask pattern is fit to a second-order polynomial to determine the pixel shifts required to eliminate the curvature. The polynomial fit is shown in Fig. 5C, and the curvature-corrected intensity profile is shown in Fig. 5B.

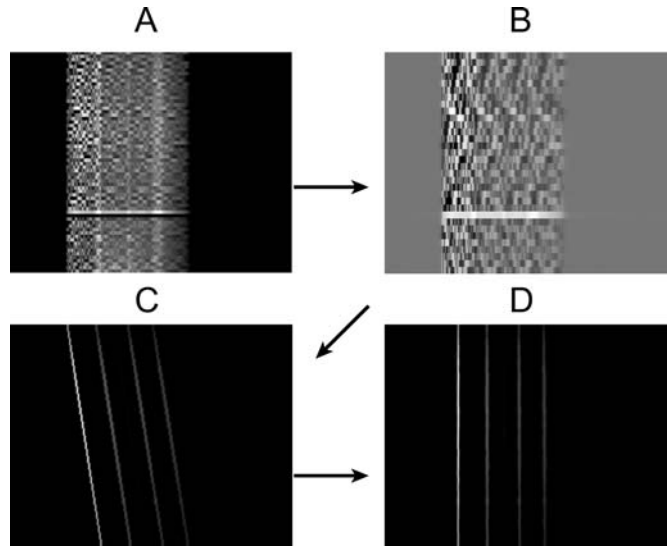

FIG. 6. (**A**) CCD data after binning by mask row. (**B**) CCD data after subtraction of complementary rows. (**C**) Spectral estimates after column-by-column inversion. (**D**) Aligned spectral estimates.

The corrected data is then selectively binned vertically to form a $2N$-row data matrix as shown in Fig. 6A. The rows used for the binning are the CCD rows that correspond to the mask rows. The complementary rows (rows added for the row doubling process) are then subtracted from their complement to form a data matrix that has N rows, shown in Fig. 6B. This matrix is now the discrete x-convolution of the Hadamard code with the input spectrum.

This relationship can be mathematically expressed as

$$\mathbf{H}_{N\times N}\mathbf{S}_{N\times M} = \mathbf{R}_{N\times M} \tag{8}$$

Here, $\mathbf{H}$ is the Hadamard matrix of order N, $\mathbf{S}$ is a matrix whose rows represent the input spectra at the columns of the input aperture, and $\mathbf{R}$ is a matrix whose rows are the row-subtracted CCD data. Inversion for $\mathbf{S}$ is then M matrix problems of size $N \times N$. We use non-negative least squares algorithms, since photon counts are always positive. The inverted cyclohexane matrix is shown in Fig. 6C. The rows of $\mathbf{S}$ have shifted spectral origins, reflecting the shifted input positions. Ideally, each adjacent estimate would be shifted exactly one horizontal mask element width; however, non-unity magnification and various other imperfections cause the shift to vary slightly. We perform a simple correlation to determine the relative shift between the rows. Using these shifts, we align the rows as shown in Fig. 6D. The N estimates are then summed to provide a further SNR advantage. Since the peak locations of cyclohexane are well known, pixel location can be mapped to wavenumber, thereby completing the calibration of the instrument.

Performance Characteristics. The resolution of the instrument was analyzed to first determine that the mask provided the expected resolution and second that the overall Raman MMS system's resolution was not broader than the linewidth of the chemical used later for quantitative analysis, ethanol. The instrument response of a Raman system is a combination of the resolution of the bare spectrometer combined with the linewidth of the excitation laser. To determine the resolution of the bare spectrometer, we measure

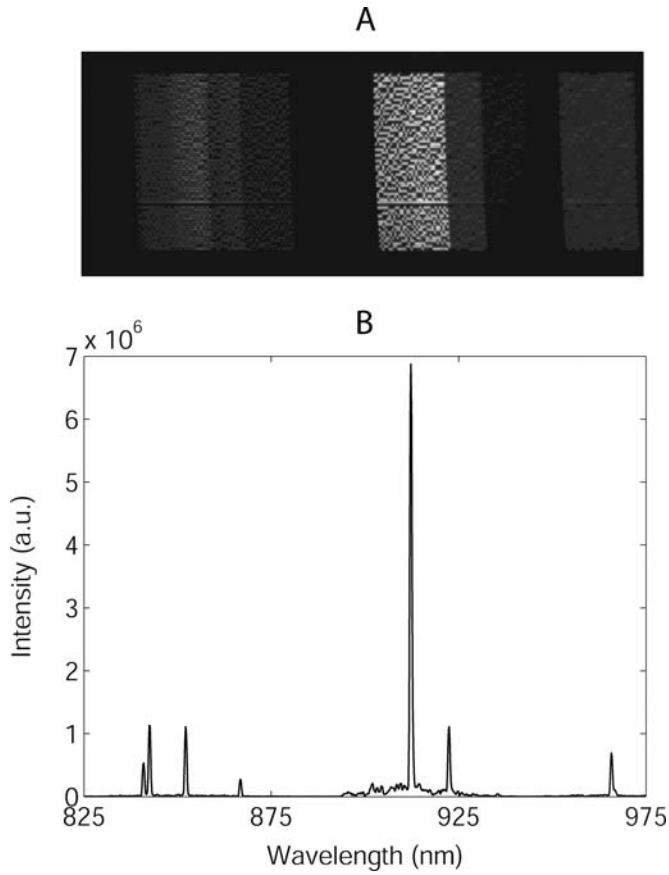

FIG. 7. (**A**) CCD image of an argon emission spectrum (1 s exposure). (**B**) Reconstructed emission spectrum of argon.

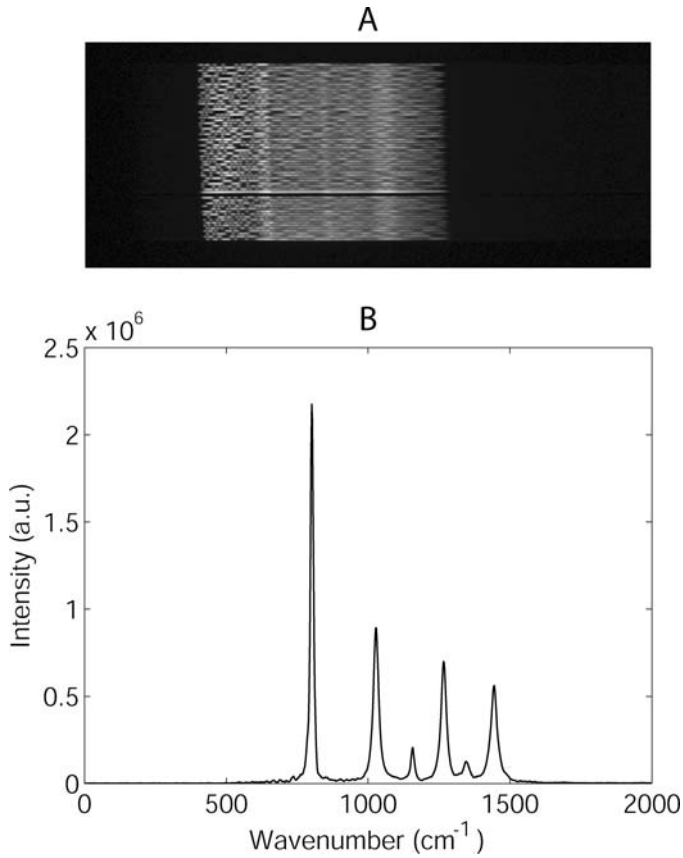

FIG. 8. (**A**) CCD image of Raman spectrum of cyclohexane (10 s exposure at 60 mW excitation power). (**B**) Reconstructed Raman spectrum of cyclohexane.

the spectrum of an Argon discharge lamp. The raw CCD image and processed spectrum for the lamp are shown in Fig. 7. Fitting a Lorentzian to the strongest peak of the spectrum allows us to determine a FWHM of 4.00 pixels, which corresponds to $\simeq$0.58 nm. Since the width of the mask features is four CCD pixels, we see that we are indeed resolution limited by the mask feature size. Thus, we have increased our throughput without sacrificing resolution.

To determine the full instrument response, we then use the instrument to measure the Raman spectrum of cyclohexane. Both the CCD image and reconstructed Raman spectrum are shown in Fig. 8. Cyclohexane has an extremely narrow Raman line, so narrow that it surely cannot be resolved by our instrument. The measured linewidth, then, is approximately the full instrument response. Fitting a Lorentzian to the narrowest peak of the cyclohexane spectrum allows us to determine a FWHM of 5.26 pixels, which corresponds to $\simeq$0.89 nm. This is equivalent to a resolution of 12.8–9.8 cm^{-1} from 500–2000 cm^{-1}, respectively. Therefore, we see that the full instrument response is broadened as a result of the linewidth of the excitation laser.

The final question is how the full instrument response compares to the linewidth of ethanol. Measuring the Raman spectrum of ethanol, we find a FWHM of 9.03 pixels. As this is less than double the Raman linewidth of the instrument, we conclude that the linewidth of ethanol is comparable to the instrument response of the MMS Raman spectrometer.

ETHANOL CHEMOMETRICS

In order to explore the use of MMS Raman spectroscopy as a noninvasive molecular estimation tool, ethanol concentration estimation in a diffuse, fluorescent medium was performed. A phantom of Intralipid was designed to have scattering properties similar to that of tissue.[26] In addition to its scattering properties, it has a significant amount of autofluorescence as well as Raman features that overlap with ethanol. Consequently, it is an excellent model for many of the challenges faced in real tissue.

Experimental Description. Our goal was to use the system to estimate the ethanol concentration in the Intralipid phantom. Cuvettes containing varying concentrations of ethanol by weight (0.008% = 1.7 mmol/L, 0.016%, 0.04%, 0.08%, 0.16%, 0.4%, and 0.8%) were prepared, and then Raman spectra were measured with the instrument. Exposure times of four minutes provided a high SNR, and six trials were performed with each sample. Data collection was automated with a Labview software program, and then the CCD images were processed into spectra by our custom codes written in Matlab. This procedure was repeated again with new samples three days later.

Regression Model and Cross-Validation. Analysis of the spectra begins with simple preprocessing. The spectra were normalized to a unit sum, since the primary cause of fluctuation in the signal is autofluorescence, which should be proportional to the laser power. The spectra were then zero-meaned to improve the modeling performance. The spectra from day 1 (before and after preprocessing) are shown in Fig. 9.

Analysis of the data proceeded by constructing a PLS model of a training data set and then using that model to predict the

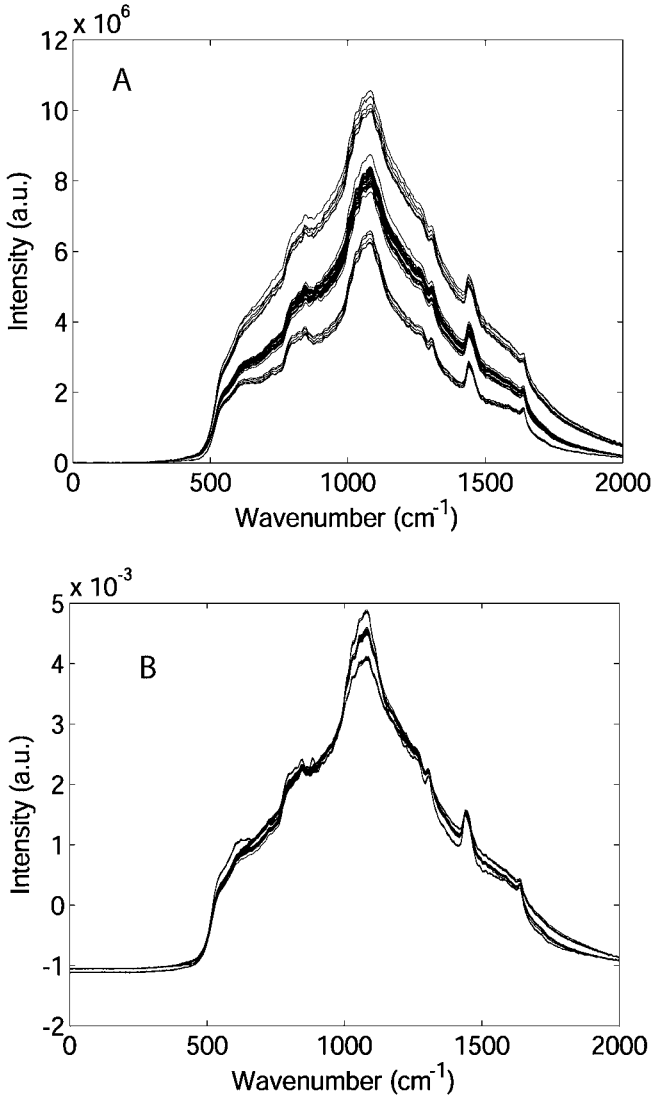

FIG. 9. (**A**) Raw, reconstructed Raman spectra of varying ethanol concentrations in Intralipid phantom. (**B**) Spectra after normalization and zero-mean scaling.

concentrations in a test data set. The goal of the model construction was to find a regression vector $\mathbf{w}$ such that $\mathbf{S} \cdot \mathbf{w} = c$, where c is the concentration of the sample with spectrum $\mathbf{S}$.[27] A sample regression vector as well as the Raman spectrum of pure ethanol is shown in Fig. 10. The method is clearly selecting wavelengths corresponding to the Raman peaks of ethanol as the primary contributors to the regression vector. The performance of the model was initially tested via leave-one-out cross-validation. In this method, a data point is selected from the data set, and a model is built from all of the remaining data points. This model was then used to estimate the concentration of the left-out data point. This process was repeated for all points in the data set.

More rigorous performance testing uses blind cross-validation. In this method a set of data points is used to form a model, and this model is then used to estimate the concentrations of a completely separate data set. In all cases, excellent performance was achieved with regression vectors formed from between 6 and 8 principal components, indicating that the algorithm is not over-fitting to noise. Examples of

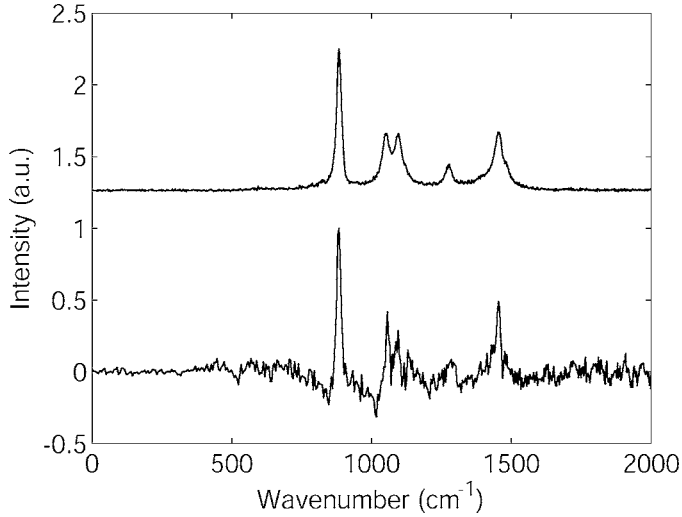

FIG. 10. (***Top***) Raman spectrum of pure ethanol (1 s exposure). (***Bottom***) PLS regression vector for day 1 data set ($r^2 = 0.42$ with ethanol spectrum).

results from leave-one-out and blind cross-validation are shown in Fig. 11. Perfect performance of the model would have the data points falling exactly on the diagonal line. We see that leave-one-out cross-validation leads to a broader spread of the data points, while blind cross-validation leads to an offset of the data points from the target line (which could potentially be corrected with a more complicated model).

For each analysis method, we computed the traditional metrics of r^2 and RMSE, as well as several relative error statistics that we feel are more accurate predictors of detection limits. The RMSE is defined as

$$\mathrm{RMSE} = \left[\frac{\sum (c_{\mathrm{est}} - c_{\mathrm{act}})^2}{k}\right]^{1/2} \tag{9}$$

where c_{est} is the estimated concentration, c_{act} is the actual concentration, and k is the number of samples. The relative error (RE) for a given data point is defined as

$$\mathrm{RE} = \frac{|c_{\mathrm{est}} - c_{\mathrm{act}}|}{c_{\mathrm{act}}} \tag{10}$$

We then compute the mean and standard deviation of the RE at each concentration, as well as the mean RE (MRE) for concentrations between 8 and 173.9 mmol/L. A summary of all the results for various combinations of training and test data sets are shown in Table I. A plot of the mean RE with error bars at ± 1 standard deviation for leave-one-out and blind cross-validation are shown in Fig. 12. Data points for concentrations below 8.7 mmol/L were suppressed on the plots due to their large relative errors. Depending on the amount of relative error one is willing to accept, we can determine a detection threshold from these plots. Making the arbitrary choice of 20% error as our threshold, we see that the system has a detection limit of between 8.7 and 17.4 mmol/L, corresponding to a concentration of between 0.04 and 0.08% by weight. For the blind cross-validation, the error is primarily from the offset observed in Fig. 11. Although the error is extremely large at the lowest concentration, the data points are still clustered in such a way as to make them distinguishable

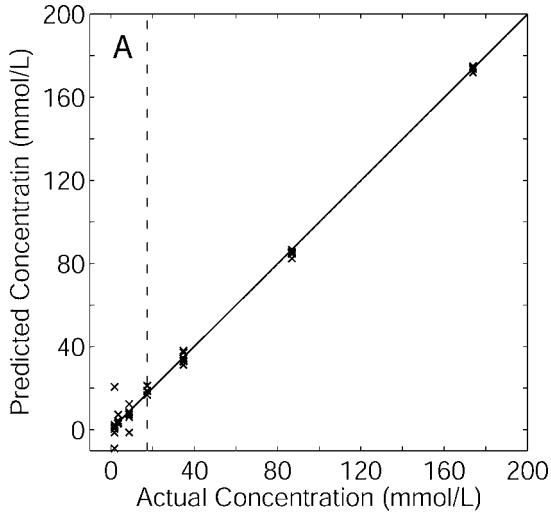

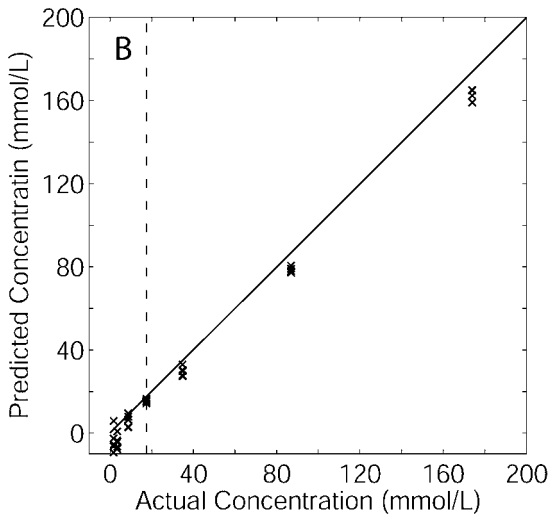

FIG. 11. (**A**) Leave-one-out cross-validation data for day 1. (**B**) Blind cross-validation for day 2, using regression vector from day 1. Dashed lines indicate one common legal intoxication limit (17.4 mmol/L = 0.08 wt. %).

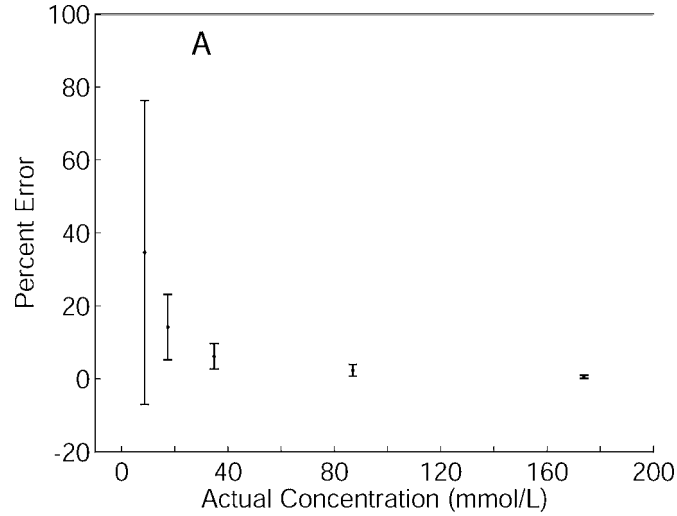

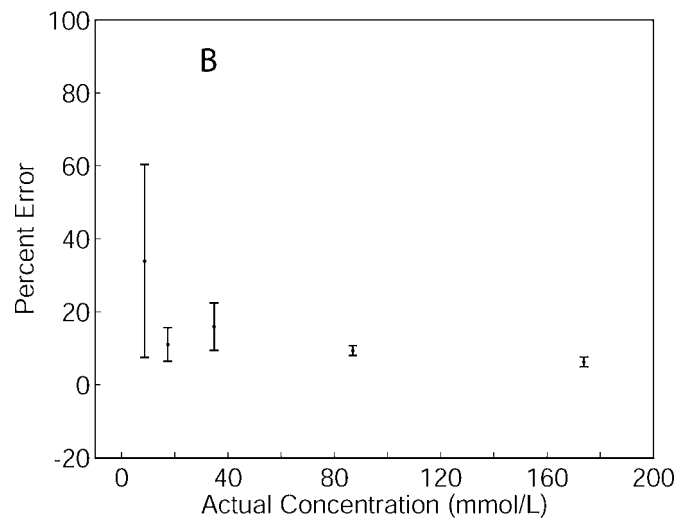

FIG. 12. (**A**) Leave-one-out cross-validation relative errors. (**B**) Blind cross-validation relative errors.

from the higher concentrations. This is reflected in the high r^2 value.

To further check the consistency of the models, we performed two more analyses. First, we combined the data from both days into a single data set and performed leave-one-out cross-validation. The results were comparable to leave-one-out cross-validation from either of the single days and required a comparable number of principal components in model formation. Second, we randomly segmented the data from both days into a training data set and test data set and used blind cross-validation. This showed improvement over blind cross-validation from either single day and demonstrates the further improvement possible when the algorithm is exposed to all forms of system variation.

TABLE I. Performance statistics for data models formed with PLS regression. The first column identifies the data sets used for model generation and testing. When the two are identical, evaluation is by leave-one-out cross-validation; otherwise blind cross-validation was used. In the last row, a random set comprising half of the data from both days was used for model generation, and the remaining data was used for evaluation. The second column indicates the number of principal components used in constructing the model. The third column indicates the r^2 correlation of the predicted values. The remaining columns show the RMSE and MRE for the full concentration range as well as the RE at two particular concentrations.

Training/test data set	*N*	r^2 value	RMSE (mmol/L)	MRE (%) 8–174 mmol/L	RE (%) at 8.7 mmol/L	RE (%) at 17.4 mmol/L
1/1	8	0.9979	2.87	11.1 ± 22.0	31.8 ± 43.7	14.8 ± 9.6
1/2	8	0.9987	6.96	15.3 ± 15.2	33.9 ± 26.5	11.1 ± 4.6
2/2	6	0.9982	2.64	9.4 ± 10.1	22.5 ± 9.86	11.1 ± 4.6
2/1	6	0.9811	15.2	63.4 ± 58.3	114.1 ± 41.0	139.8 ± 6.2
1+2/1+2	8	0.9965	3.62	12.3 ± 31.9	40.8 ± 63.3	10.4 ± 6.7
Rand./Comp.	8	0.998	3.55	9.2 ± 9.8	21.0 ± 12.2	12.4 ± 9.6

CONCLUSION

We have demonstrated that MMS systems can statically measure the average spectrum of a diffuse source with a large collection aperture and can be used to quantitatively estimate concentrations of ethanol at physiological concentrations in a tissue-like phantom. For sources of large étendue, collection efficiencies can be greatly increased over slit-based dispersive spectrometers, where spatial filtering is used to eliminate the spatio-spectral ambiguity. By choosing aperture masks that have columns of orthogonal functions, spectral reconstruction is rapidly accomplished with a high fidelity. Through leave-one-out and blind cross-validation, detection limits of between 8.7 and 17.4 mmol/L have been demonstrated with an excitation power of 60 mW, only twice the permissible ANSI standard for human tissue. With this gain in sensitivity, the possibility for noninvasive *in vivo* chemometrics is greatly advanced.

ACKNOWLEDGMENTS

This work was supported by the National Institute on Alcohol Abuse and Alcoholism through the Integrated Alcohol Sensing and Data Analysis program under contract N01-AA-23013. The technical assistance of E. Diebold is greatly appreciated. We would also like to thank B. D. Guenther, P. Potuluri, and M. E. Sullivan for stimulating discussions.

1. E. B. Hanlon, R. Manoharan, T. W. Koo, K. E. Shafer, J. T. Motz, M. Fitzmaurice, J. R. Kramer, I. Itzkan, R. R. Dasari, and M. S. Feld, Phys. Med. Biol. **45,** 1 (2000).
2. X. Dou, Y. Yamaguchi, H. Yamamoto, S. Doi, and Y. Ozaki, Vib. Spectrosc. **13,** 83 (1996).
3. J. Y. Qu, B. C. Wilson, and D. Suria, Appl. Opt. **38,** 5491 (1999).
4. C. C. Pelletier, J. L. Lambert, and M. Borchert, Appl. Spectrosc. **59,** 1024 (2005).
5. A. M. K. Enejder, T. W. Koo, J. Oh, M. Hunter, S. Sasic, M. S. Feld, and G. L. Horowitz, Opt. Lett. **27,** 2004 (2002).
6. A. M. K. Enejder, T. G. Scecina, J. Oh, M. Hunter, W. C. Shih, S. Sasic, G. L. Horowitz, and M. S. Feld, J. Biomed. Opt. **10,** 031114 (2005).
7. P. Matousek, I. P. Clark, E. R. C. Draper, M. D. Morris, A. E. Goodship, N. Everall, M. Towrie, W. Finney, and A. Parker, Appl. Spectrosc. **59,** 393 (2005).
8. M. J. E. Golay, J. Opt. Soc. Am. **39,** 437 (1949).
9. H. M. P. Phillips, T. Fine, and N. Sloane, Appl. Opt. **9,** 1149 (1970).
10. J. J. Decker, Appl. Opt. **10,** 510 (1971).
11. M. Harwit and N. J. A. Sloane, *Hadamard Transform Optics* (Academic Press, New York, 1979), pp. 44–95.
12. D. C. Tilotta, R. D. Freeman, and W. G. Fateley, Appl. Spectrosc. **41,** 1280 (1987).
13. D. C. Tilotta, R. M. Hammaker, and W. G. Fateley, Appl. Spectrosc. **41,** 727 (1987).
14. Q. S. Hanley, P. J. Verveer, and T. M. Jovin, Appl. Spectrosc. **53,** 1 (1999).
15. Q. S. Hanley and T. M. Jovin, Appl. Spectrosc. **55,** 1115 (2001).
16. R. Riesenberg and U. Dillner, "Imaging Spectrometry V", Proc. SPIE-Int. Soc. Opt. Eng. **3753,** 203 (1999).
17. S. B. Mende, E. S. Claflin, R. L. Rairden, and G. R. Swenson, Appl. Opt. **32,** 7095 (1993).
18. M. E. Gehm, S. T. McCain, N. P. Pitsianis, D. J. Brady, P. Potulri, and M. E. Sullivan, "Static 2D Aperture Coding for Multimodal Multiplex Spectroscopy", Appl. Opt., paper in press (2006).
19. T. Vo-Dinh, *Biomedical Photonics Handbook* (CRC Press, Boca Raton, FL, 2003), pp. 2-1–2-75.
20. D. J. Brady, Opt. Lett. **27,** 16 (2002).
21. M. G. Shim and B. C. Wilson, J. Raman Spectrosc. **28,** 131 (1997).
22. Z. Huang, H. Zeng, I. Hamzavi, D. I. McLean, and H. Lui, Opt. Lett. **26,** 1782 (2001).
23. R. A. L. Tolboom, N. J. Dam, and H. T. Meulen, Appl. Opt. **43,** 5682 (2004).
24. R. J. Scheuplein and I. H. Blank, Phys. Rev. **51,** 702 (1971).
25. D. J. Schroeder, *Astronomical Optics* (Academic Press, London, England, 1987), pp. 261–262.
26. H. J. Vanstaveren, C. J. M. Moes, J. Vanmarle, S. A. Prahl, and M. J. C. Vangemert, Appl. Opt. **30,** 4507 (1991).
27. H. Martens and T. Næs, *Multivariate Calibration* (John Wiley and Sons, Chichester, U.K., 1989), pp. 73–236.
28. A. Roggan, M. Friebel, K. Dorschel, A. Hahn, and G. Muller, J. Biomed. Opt. **4,** 36 (1999).